A nitroaromatic cathode with an ultrahigh energy density based on six-electron reaction per nitro group for lithium batteries

Zifeng Chen[a], Hai Su[a], Pengfei Sun[a], Panxing Bai[a], Jixing Yang[a], Mengjie Li[a], Yunfeng Deng[b], Yang Liu[c], Yanhou Geng[b,d], and Yunhua Xu[a,1]

[a]School of Materials Science and Engineering, Key Laboratory of Advanced Ceramics and Machining Technology (Ministry of Education) and Tianjin Key Laboratory of Composite and Functional Materials, Tianjin University, Tianjin 300072, People's Republic of China; [b]School of Materials Science and Engineering and Tianjin Key Laboratory of Molecular Optoelectronic Science, Tianjin University, Tianjin 300072, People's Republic of China; [c]Institute for Chemical Drug Control, National Institutes for Food and Drug Control, Beijing 102625, People's Republic of China; and [d]Joint School of National University of Singapore and Tianjin University, International Campus of Tianjin University, Fuzhou 350207, People's Republic of China

Edited by Alexis Bell, Department of Chemical and Biomolecular Engineering, University of California, Berkeley, CA; received September 12, 2021; accepted November 22, 2021

Organic electrode materials have emerged as promising alternatives to conventional inorganic materials because of their structural diversity and environmental friendliness feature. However, their low energy densities, limited by the single-electron reaction per active group, have plagued the practical applications. Here, we report a nitroaromatic cathode that performs a six-electron reaction per nitro group, drastically improving the specific capacity and energy density compared with the organic electrodes based on single-electron reactions. Based on such a reaction mechanism, the organic cathode of 1,5-dinitronaphthalene demonstrates an ultrahigh specific capacity of 1,338 mAh·g^{-1} and energy density of 3,273 Wh·kg^{-1}, which surpass all existing organic cathodes. The reaction path was verified as a conversion from nitro to amino groups. Our findings open up a pathway, in terms of battery chemistry, for ultrahigh-energy-density Li-organic batteries.

Li-organic battery | organic electrode material | nitroaromatic compound | six-electron reduction | high energy density

With the rapid development of social economy, the demand for high-energy-density storage systems is ever increasing, particularly in the fields of military, aerospace, medical, and civilian applications. Lithium-ion batteries (LIBs) have been extensively explored as high-energy-density storage devices (1–4). Commercial LIBs use crystalline transition metal oxide cathodes, such as $LiCoO_2$, $LiMnO_2$, and $LiNi_xMn_yCo_{1-x-y}O_2$ (5–12). They store energy via insertion/extraction of Li ions, which highly depends on the crystal structure and limits their capacities and energy densities (<300 mAh·g^{-1} with energy density of <1,000 Wh·kg^{-1}). Some new battery systems with conversion reaction cathodes, such as Li-S (2,600 Wh·kg^{-1}) and Li-O_2 (3,450 Wh·kg^{-1}) batteries (13–19), have been extensively investigated due to their high theoretical energy densities. However, they suffer from serious dissolution, interfacial stability, and/or side reaction issues, and the practical energy densities are much lower than their theoretical values.

Compared with the aforementioned rechargeable batteries, lithium primary batteries can provide remarkably higher energy densities. For example, lithium-fluorinated carbon (Li-CF_x) batteries use a CF_x cathode that has a high theoretical energy density of 2,180 Wh·kg^{-1}, which is the highest value among all commercial cathode materials in lithium batteries (20–22). Recently, it is reported that, different from the formation of crystal LiF in liquid electrolytes, amorphous LiF was produced and uniformly distributed on the carbon matrix when a solid-state electrolyte was used (23). This may enable a reversible electrochemical reactivity of CF_x with lithium and provide a possibility for high-energy-density batteries. Nevertheless, CF_x must be synthesized in harsh conditions with precise control, leading to high cost and hindering the wide application (20). Some liquid and gas cathodes, such as SO_2, $SOCl_2$, and SF_6 (24–27), can also offer high energy densities, but they tend to be volatile and induce severe safety hazards, especially on the occasion of thermal runaway. Therefore, it is highly desired to develop feasible and reliable battery systems with high energy density.

Organic electrode materials offer many merits compared with inorganic electrode materials, including structure diversity and designability, abundance of raw materials, relatively easy synthesis, and environmental friendliness (28–35). Their energy storage processes rely on the uptake of cations or anions on the active groups, such as carbonyl group, quaternary nitrogen, and nitroxyl radical (36–40). Most of them undergo one electron reaction, leading to limited specific capacity and energy density (Fig. 1). For example, one carbonyl group (C=O) can be converted into C-OLi structure via accepting one electron and one lithium ion (36), providing a theoretical specific capacity of 957 mAh·g^{-1} (based on the mass of functional group as marked by dashed circle in Fig. 1). If considering the inactive components, insulating property, and high solubility of organic molecules, most organic electrode materials exhibit inferior specific capacities. Although a high specific capacity of 902 mAh·g^{-1} was

Significance

Organic electrode materials have shown great potential in lithium batteries in terms of easy synthesis, raw materials abundance, and environmental friendliness. However, the traditional organic electrodes typically experience single-electron reaction per active group, leading to limited specific capacities and energy densities. Herein, we report a battery chemistry of a nitroaromatic cathode, in which six-electron transfer occurs on each nitro group, resulting in an ultrahigh specific capacity and energy density, higher than all existing organic electrode materials and even most inorganic electrode materials.

Author contributions: Z.C. and Y.X. designed research; Z.C., H.S., P.S., J.Y., and Y.L. performed research; Y.D., Y.L., and Y.G. contributed new reagents/analytic tools; Z.C., H.S., P.S., P.B., J.Y., M.L., Y.D., Y.L., Y.G., and Y.X. analyzed data; and Z.C. and Y.X. wrote the paper.

The authors declare no competing interest.

This article is a PNAS Direct Submission.

[1]To whom correspondence may be addressed. Email: yunhua.xu@tju.edu.cn.

This article contains supporting information online at http://www.pnas.org/lookup/suppl/doi:10.1073/pnas.2116775119/-/DCSupplemental.

Published January 31, 2022.

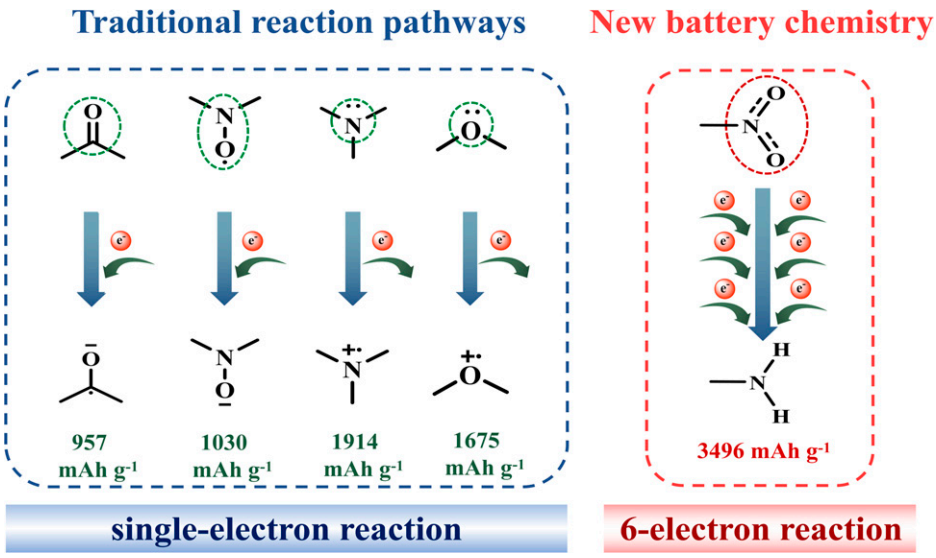

Fig. 1. Reaction mechanisms of organic groups in batteries.

gained for cyclohexanehexone in LIBs, its high solubility induces significant challenges in practical applications (41). Recently, a Li-containing organic compound, dilithium 1,4-phenylenebis ((methylsulfonyl) amide) (Li_2-*p*-PDSA) was synthesized, offering a new design for organic electrode materials, while it still follows the single-electron reaction path per electroactive group and shows a low specific capacity of 194 mAh·g^{-1} (42). Therefore, new battery system needs to be developed to take full advantage of organic electrode materials for high-energy-density LIBs.

In this work, we report a battery chemistry of six-electron reduction on nitro group ($-NO_2$) of nitroaromatic cathode. Based on such a reaction, 1,5-dinitronaphthalene (1,5-DNN; Fig. 2*A*) as a cathode in LIBs achieves an ultrahigh specific capacity of 1,338 mAh·g^{-1} and energy density of 3,273 Wh·kg^{-1}. This is a record for organic electrode materials, even higher than inorganic electrode materials. It is identified that nitro groups are reduced to amino groups through a six-electron transfer reaction via multiple characterization techniques. Our findings provide a path for achieving high-energy-density Li-organic batteries.

Results and Discussion

The electrochemical performance of 1,5-DNN was evaluated in coin-type cells using Li metal as the counter electrode and the electrolyte of 0.5 M lithium perchlorate ($LiClO_4$) in 1,2-dimethoxyethane (DME) with 10 vol% fluoroethylene carbonate (FEC). Galvanostatic charge/discharge (current density: 20 mA·g^{-1}) and cyclic voltammetry measurements (CV) (scan rate: 0.01 mV·s^{-1}) were performed in a voltage window of 3.0 V to 2.0 V. The voltage profile shows two long discharge voltage plateaus at 2.55 V and 2.45 V with an ultrahigh specific capacity of 1,338 mAh·g^{-1} (Fig. 2*B*). However, no reversible capacity is measured in the following charge process (Fig. 2*B*), suggesting an irreversible electrochemical reduction of 1,5-DNN. The corresponding CV curve exhibits a sharp peak at 2.44 V with a broad wave around 2.34 V, while no oxidation peak is measured during the subsequent anodic scan (*SI Appendix*, Fig. S1). Remarkably, an impressive energy density of 3,273 Wh·kg^{-1} is demonstrated (Fig. 2*C*), which surpasses all organic and inorganic cathode materials (Fig. 2*D* and *SI Appendix*, Table S1). The electrochemical performance of 1,5-DNN was also tested at an elevated temperature of 60 °C. Higher specific capacity of 1,387 mAh·g^{-1} and energy density of 3,930 Wh·kg^{-1} are obtained (*SI Appendix*, Fig. S2).

The self-discharge behavior of 1,5-DNN electrode material was evaluated (*SI Appendix*, Fig. S3). After 3-mo storage at room temperature, there is no capacity fading of the 1,5-DNN–based batteries, suggesting stable shelf storage. Meanwhile, the shelf storage performance of partially discharged batteries was also examined (*SI Appendix*, Fig. S4), and no obvious capacity loss is detected after 1-wk storage.

The electrochemical performance was also examined in an FEC-free electrolyte of 0.5 M $LiClO_4$ in DME in the same conditions as those for the FEC-containing electrolyte (*SI Appendix*, Fig. S5). In CV profiles (*SI Appendix*, Fig. S5*A*), a pronounced anodic peak at 2.37 V is presented, and a cathodic peak at 2.55 V is measured. Correspondingly, 1,5-DNN shows a distinct discharge plateau at 2.39 V with a specific capacity of 413 mAh·g^{-1} in the galvanostatic charge/discharge voltage profiles and a charge plateau at 2.45 V with a capacity of 221 mAh·g^{-1} (*SI Appendix*, Fig. S5*B*). The entirely different electrochemical behaviors suggest disparate storage mechanisms in the two electrolytes. Fourier transform infrared (FTIR) spectra of 1,5-DNN electrodes at different charge/discharge states were recorded in the FEC-free electrolyte (*SI Appendix*, Fig. S5*C*). Two characteristic nitro stretching bands at 1,495 cm^{-1} and 1,338 cm^{-1} are displayed for the pristine electrodes. At the fully discharged state of 2.0 V, those peaks disappear, and a new peak at 1,384 cm^{-1} appears, indicating the formation of lithiated nitro anions (43). A reverse change behavior is observed with the reformation of nitro groups upon charging. These results clearly reveal an electrochemical transformation between nitro groups and lithiated nitro anions during cycling in the FEC-free electrolyte (*SI Appendix*, Fig. S5*D*).

To understand the FEC effects on the energy storage properties of 1,5-DNN, the electrochemical process was investigated in electrolytes with different contents of FEC from 0 to 50% (Fig. 3*A*). The discharge voltage increases from 2.39 V in the FEC-free electrolyte to 2.55 V in the FEC-containing electrolyte. Besides, the discharge capacity gradually increases from 413 mAh·g^{-1} for the FEC-free electrolyte to 1,338 mAh·g^{-1} for the FEC-containing electrolyte. The decrease in discharge capacities with increasing contents of FEC (>10%) should be associated with the poor wettability of electrolytes to polypropylene (PP) separators (44). Meanwhile, different colors are displayed for the separators at a discharge state of 2.0 V in the electrolytes with and without FEC (Fig. 3*B*). For the FEC-free electrolyte, the separator shows a dark purple color, while it is

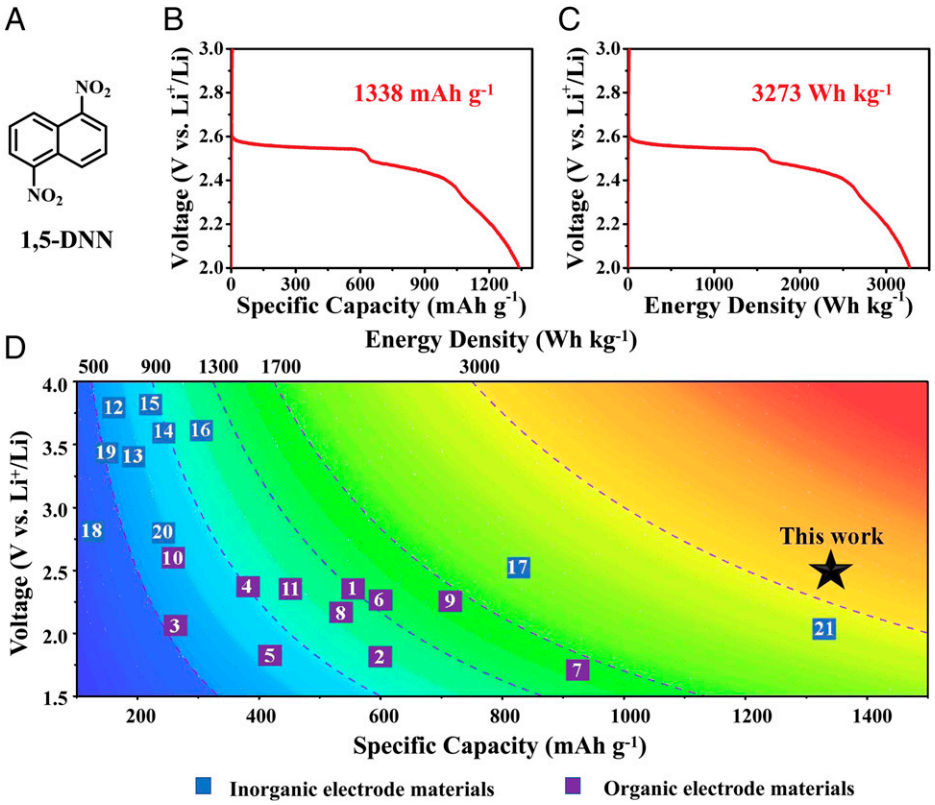

Fig. 2. Electrochemical performance of 1,5-DNN. (*A*) Chemical structure of 1,5-DNN. (*B* and *C*) Galvanostatic charge/discharge profiles of 1,5-DNN. (*D*) Performance comparison of 1,5-DNN with reported organic/inorganic electrode materials in terms of energy density, specific capacity and voltage. Cathodes for comparison (references): 1, *p*-DNB (43); 2, $Li_2C_6O_6$ (49); 3, P14AQ (50); 4, PTO (51); 5, 3Q (31); 6, AQ (44); 7, C_6O_6 (41); 8, *o*-DNB (43); 9, *m*-DNB (43); 10, 4,5-PhenQ (51); 11, C4Q (52); 12, $LiCoO_2$ (53); 13, $LiFePO_4$ (54); 14, NCA (55); 15, NCM-811 (56); 16, Li-rich (57); 17, CF_x (21); 18, MnO_2 (58); 19 $SOCl_2$ (59), 20 SO_2 (24); 21, S (60).

pale yellow for the FEC-containing electrolyte, indicating that different reduction products are generated in different electrochemical processes between the two electrolytes.

The difference is also observed in morphology of the discharged electrodes. The morphology of the pristine and discharged electrodes in the FEC-free and FEC-containing electrolytes was checked by scanning electron microscope (SEM). The pristine electrode shows that the active 1,5-DNN particles are well wrapped within graphene sheets (*SI Appendix*, Fig. S6*A*). However, after discharging in the FEC-free electrolyte, no active compound is displayed (*SI Appendix*, Fig. S6*B*), which should be caused by the high solubility of the reduction products of lithiated nitro anions. In sharp contrast, a large number of particles are produced during discharging in the FEC-containing electrolyte (*SI Appendix*, Fig. S6 *C–F*), identifying a different reduction path.

To gain insights in the reduction mechanism of 1,5-DNN, the cycled electrodes with the FEC-containing electrolyte were further examined by X-ray photoelectron spectroscopy (XPS) and gas chromatography mass spectrometry (GC-MS). The high-resolution XPS spectra of N 1s at different discharge states are presented in Fig. 3*C*. The pristine 1,5-DNN electrode presents a characteristic peak of $-NO_2$ at 406.2 eV, with a satellite peak at 400.2 eV. Upon discharging, the signal of $-NO_2$ gradually decreases, but the peak of the amino group ($-NH_2$) at 399.7 eV appears, verifying the reduction from nitro to amino groups. At the fully discharged state of 2.0 V, no signal of $-NO_2$ is detected, suggesting a complete conversion from $-NO_2$ to $-NH_2$. The amino group is also verified by GC-MS. When discharged to 500 mAh·g^{-1} on the first discharge plateau, a distinct peak at m/z = 188.1 is observed, which is ascribed to 5-nitronaphthalen-1-amine (5-NN-1-A) (Fig. 3*D*), an intermediate product during the reduction. At the fully discharged state of 2.0 V, the presence of the peak at m/z = 158.1 affirms the generation of 1,5-naphthalenediamine (1,5-NDA) (Fig. 3*E*). To gain further information about the reduction products, the electrochemical performance of 1,5-NDA was examined in the FEC-containing electrolyte and the same measurement conditions with those for 1,5-DNN. Negligible specific capacity is delivered (*SI Appendix*, Fig. S7), implying that 1,5-NDA cannot be reduced further and thereby is the final reduction product of 1,5-DNN during the electrochemical reduction process. Clearly, the above results imply that $-NO_2$ is reduced to $-NH_2$ by protons (H^+). The possible transformation mechanism of $-NO_2$ to $-NH_2$ is illustrated in *SI Appendix*, Scheme S1.

The concentration effects of FEC were studied by examining the reduced 1,5-DNN in the electrolytes with different contents of FEC from 10 to 50% via FTIR. The 1,5-DNN electrodes were partially discharged to 200 mAh·g^{-1} and retrieved for testing (*SI Appendix*, Fig. S8). At high contents of > 20%, the presence of the C–H stretching vibration peak at 2,956 cm^{-1} suggests the generation of vinylene carbonate (VC). The absence of VC signal at low FEC contents should be due to the too low concentration of VC produced in the reduction, which exceeds the detection limit of the experimental instrument. It is hypothesized that the transformation from FEC to VC would be accompanied by the generation of a large amount of HF, which then reacts with Li ions to form LiF. The formation of LiF is verified by the distinct peak of LiF at 685.6 eV in the high-resolution F 1s XPS spectrum (Fig. 4*A*) and three characteristic X-ray diffraction (XRD) peaks at around 38.7°, 45.0°, and 65.5° (marked with red stars) for the fully discharged electrode (Fig. 4*B*).

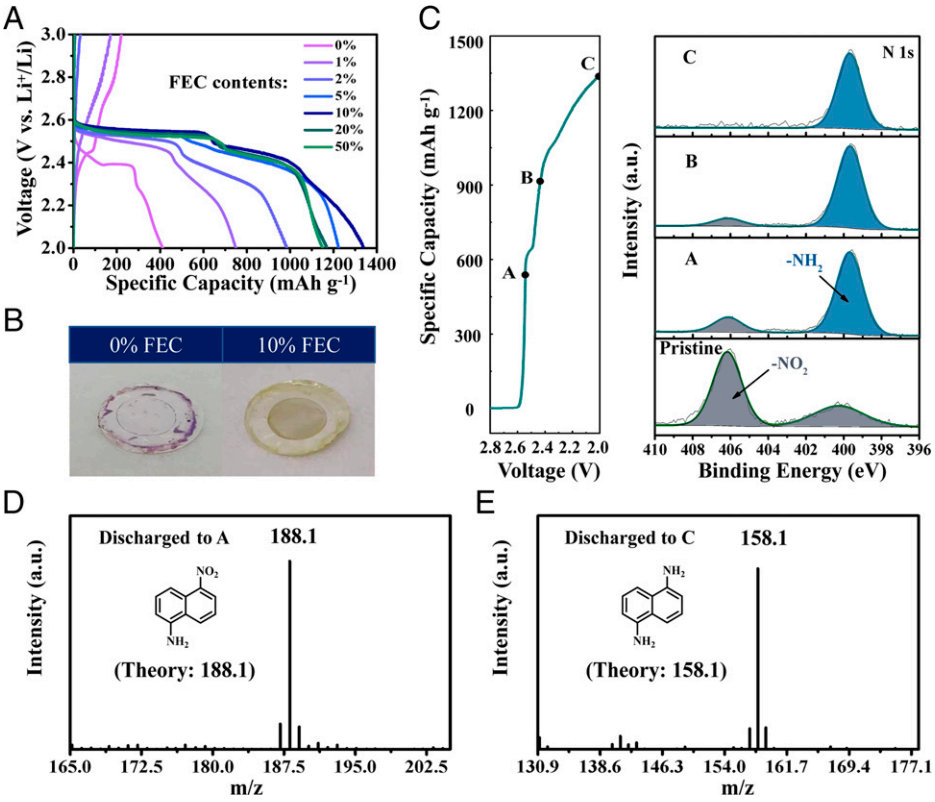

Fig. 3. Reaction mechanism of 1,5-DNN. (*A*) Galvanostatic charge/discharge profiles of 1,5-DNN in the electrolytes with FEC contents ranging from 0 to 50%. (*B*) Digital photographs of separators retrieved at 2-V discharged state in the electrolytes without/with FEC. (*C*) Voltage–capacity profile of 1,5-DNN with marked points for XPS tests and corresponding ex situ N 1s XPS spectra. (*D* and *E*) GC-MS spectra of discharged 1,5-DNN electrodes.

It is well known that VC is easy to reduce on discharge to produce vinyloxy radical anions and carbon dioxide (CO_2) (45, 46). The former can react with Li^+ and initiate the polymerization of VC to generate organic lithium salts (ROCOOLi), while CO_2 can react with water (H_2O) (originating from the trace amount of water in the electrolyte and/or the reduction product of 1,5-DNN) to produce carbonic acid (H_2CO_3). Protons would participate in the reduction of 1,5-DNN, and CO_3^{2-} would react with Li^+ to form Li_2CO_3. Note that CO_2 can also be reduced to $Li_2C_2O_4$ in the presence of Li^+ (45). These reduction products are clearly detected by the XPS measurements on the fully discharged electrode, taking the pristine 1,5-DNN electrode as a reference (*SI Appendix*, Fig. S9). The resulting lithium salts of ROCOOLi, Li_2CO_3, and $Li_2C_2O_4$ are clearly indicated in the high-resolution C 1s spectrum by the peaks at 290.3, 289.9, and 287.1 eV, respectively (Fig. 4*C*). The pronounced peak of Li_2CO_3 at 531.4 eV is also observed in the high-resolution O 1s spectrum (Fig. 4*D*). The generation of Li_2CO_3 and $Li_2C_2O_4$ is further verified by the characteristic peaks at 1,408 and 1,653 cm^{-1} in the FTIR spectra of the electrodes at different discharge states (Fig. 4*E*). A large number of products are also observed in the SEM images of the cycled electrodes at different discharge states (*SI Appendix*, Fig. S6). This is also reflected in the increasing impedance during discharging due to the deposition of reduction products on the electrodes (*SI Appendix*, Fig. S10).

According to the aforementioned analysis, the reduction process of 1,5-DNN in the presence of FEC is outlined in Fig. 5. The defluorination of FEC generates HF and VC. The former reacts with Li^+ in the electrolytes to form LiF, and the dissociated protons participate in the reduction of 1,5-DNN. VC is then further reduced to vinyloxy radical anions and CO_2. The vinyloxy radical anions initiate the polymerization of VC to generate ROCOOLi, while CO_2 reacts with H_2O to produce H_2CO_3. Protons dissociated from H_2CO_3 can also participate in the reduction of 1,5-DNN accompanied by the formation of Li_2CO_3 via the reaction of CO_3^{2-} with Li^+. CO_2 can also be directly reduced to $Li_2C_2O_4$. Therefore, 1,5-DNN is reduced to 5-NN-1-A and 1,5-NDA in two steps in the presence of protons.

To prove the function of VC in the reduction of 1,5-DNN, VC was directly used as an electrolyte additive instead of FEC. Cells were assembled using 1,5-DNN electrode and the electrolyte of 0.5 M $LiClO_4$ in DME with 10% VC. A high discharge specific capacity of 827 $mAh{\cdot}g^{-1}$ is achieved with two voltage plateaus of 2.48 and 2.31 V (Fig. 6*A*), consistent with the results of the FEC-containing electrolyte. Correspondingly, CV measurement shows two reduction peaks at 2.38 and 2.27 V during the first cathodic scan (*SI Appendix*, Fig. S11). The same color change of separator occurs for the VC-containing electrolyte as for the FEC-containing electrolyte at fully discharged state (*SI Appendix*, Fig. S12). But LiF generated with the FEC-containing electrolyte, 5-NN-1-A, Li_2CO_3, $Li_2C_2O_4$, and ROCOOLi are measured by GC-MS, XPS, and FTIR for the VC-containing electrolyte (Fig. 6*B* and *SI Appendix*, Figs. S13–S15), consistent with those observations with the FEC-containing electrolyte. Therefore, it can be concluded that VC can promote the same reduction from $-NO_2$ to $-NH_2$ as FEC.

Compared with the capacity in the FEC-containing electrolyte, the lower discharge capacity of the VC-containing electrolyte should be caused by the insufficient protons in the system. To enhance the proton supply, 1% water was added into the VC-containing electrolyte. As predicted, a much higher discharge capacity of 1,079 $mAh{\cdot}g^{-1}$ is obtained (*SI Appendix*, Fig. S16), revealing a key role of protons in the reduction of 1,5-DNN.

The proposed reduction path of 1,5-DNN illustrates that protons participate in the discharge reaction, in which CO_2 may serve as a reactant to produce protons. Therefore, open cells

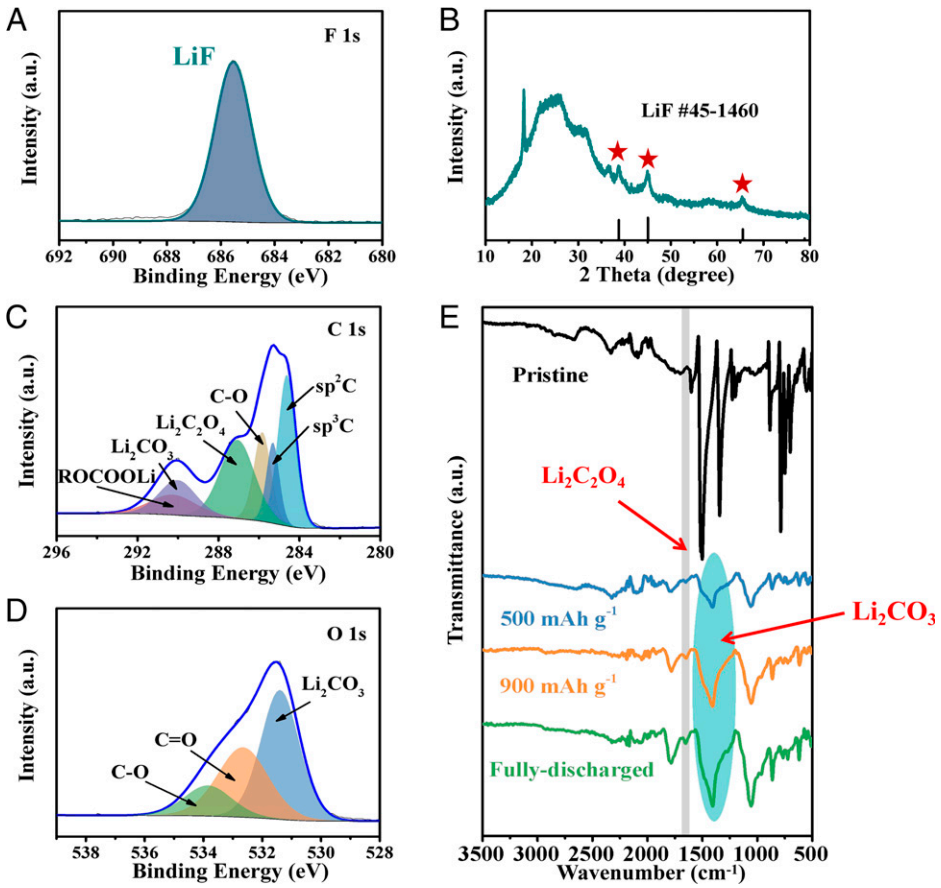

Fig. 4. (*A*) High-resolution F 1s XPS spectrum and (*B*) XRD pattern of fully discharged 1,5-DNN electrode. High-resolution (*C*) C 1s and (*D*) O 1s XPS spectra of discharged (2 V) 1,5-DNN electrodes. (*E*) FTIR spectra of 1,5-DNN electrodes at different discharge states.

were fabricated using an additive-free electrolyte of 0.5 M $LiClO_4$ in tetraethylene glycol dimethyl ether (TEGDME) but operated in a CO_2 environment (*SI Appendix*, Fig. S17), similar to Li-CO_2 batteries (47, 48). Excitingly, a high specific capacity of 960 mAh·g^{-1} is delivered with similar electrochemical behaviors (Fig. 6*C*), as well as the same reduction products as those probed in the FEC and VC-containing electrolytes (Fig. 6*D* and *SI Appendix*, Figs. S18 and S19). Interestingly, if the cell is operated in argon atmosphere, a different redox process occurs from that in CO_2 atmosphere (*SI Appendix*, Fig. S20). These results highlight the reduction path of 1,5-DNN with CO_2 which participates in the production of protons and provide a clear figure of the understanding of the high energy reduction.

In conclusion, we report a battery chemistry using 1,5-DNN as an organic cathode material. An ultrahigh specific capacity of 1,338 mAh·g^{-1} was delivered with an ultrahigh energy density of 3,273 Wh·kg^{-1}, which exceeds all cathode materials reported previously. Various characterization methods were conducted to explore the electrochemical process of 1,5-DNN. The results show that nitro groups of 1,5-DNN are reduced to amino groups through six-electron transfer during discharging, accompanied by the generation of inorganic and organic lithium salts (LiF, Li_2CO_3, $Li_2C_2O_4$, and ROCOOLi). This battery chemistry provides a pathway to realize the practical use of high-energy-density organic electrode materials.

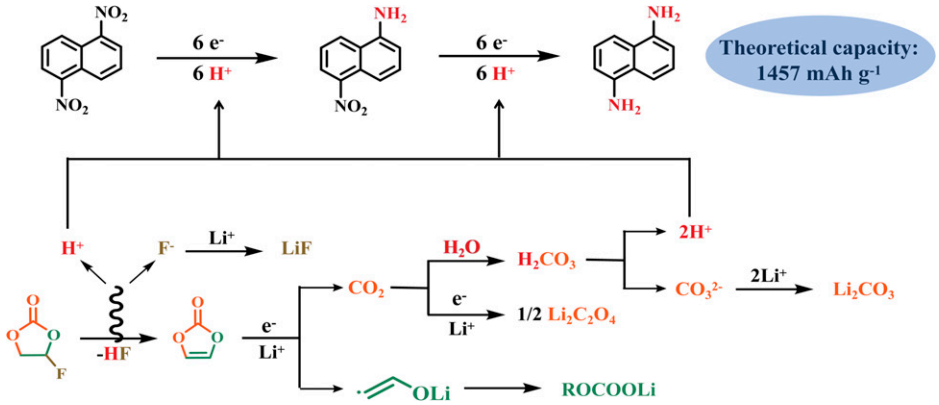

Fig. 5. Supposed reduction path of 1,5-DNN.

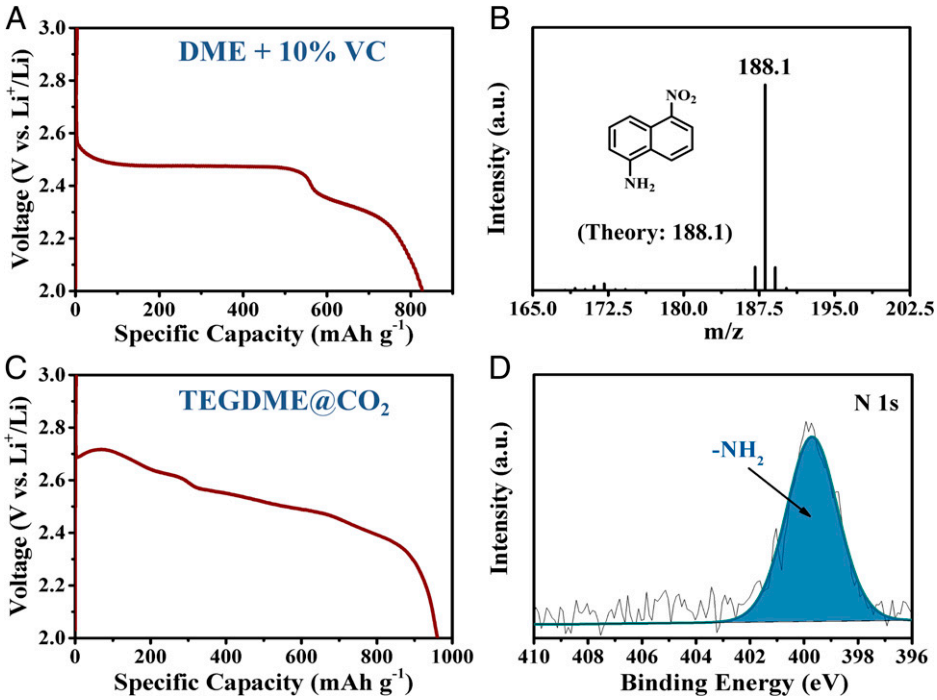

Fig. 6. (*A*) Galvanostatic charge/discharge profiles of 1,5-DNN in the VC-containing electrolyte. (*B*) GC-MS spectra of 1,5-DNN electrodes when discharged to 400 mAh·g^{-1}. (*C*) Galvanostatic charge/discharge profiles of 1,5-DNN in the TEGDME electrolyte in CO_2 atmosphere. (*D*) High-resolution N 1s XPS spectra of 2-V discharged 1,5-DNN electrode in CO_2 atmosphere in the TEGDME electrolyte.

Materials and Methods

Materials. 1,5-DNN (97%) and 1,5-NDA (99%) were purchased from Shanghai Aladin Biochemical Technology Co., Ltd. and Energy Chemical, respectively. $LiClO_4$ (99.99%, metal basis) was purchased from Shanghai Aladin Biochemical Technology Co., Ltd. Battery-grade DME, FEC, and VC were purchased from Guangdong Canrd New Energy Technology Co., Ltd. TEGDME (≥99%) was purchased from Sigma-Aldrich, Co. For the FEC-containing or VC-containing electrolytes, calculated amounts of $LiClO_4$ and DME were mixed, then 10% FEC or VC (by the volume of DME) were added into the mixture and stirred for half an hour. The FEC-free or TEGDME electrolytes were obtained simply by mixing the $LiClO_4$ with DME or TEGDME. All procedures were performed in Ar-filled gloveboxes with the O_2 and H_2O levels less than 0.1 ppm.

Electrode Preparation and Electrochemical Tests. 1,5-DNN and 1,5-NDA electrodes were prepared by mixing 1,5-DNN (or 1,5-NDA) compounds, graphene, and sodium alginate aqueous solution (15 mg·mL^{-1}) in a ratio of 6:3:1 (wt%) to form a slurry that was cast on aluminum foil by a doctor blade. The mixture was dried under vacuum at 50 °C for 8 h. CR 2032 coin-type cells were fabricated in a glovebox filled with argon (Ar) (O_2 < 0.1 ppm, H_2O < 0.1 ppm) using lithium metal as counter electrodes, PP separators, and electrolytes of 20 μL of 0.5 M $LiClO_4$ in DME or DME with 10% FEC (or VC). For the batteries using 0.5 M $LiClO_4$ in TEGDME as the electrolyte, Whatman GF/C microfiber filters were used as separators. Specifically, CR 2032 with several punched holes in a cathode was used to fabricate the cells operated in CO_2 atmosphere. All charge/discharge tests were conducted on a NEWARE battery test system in a voltage range of 3.0 V to 2.0 V, with a current density of 20 mA·g^{-1}. CV measurements were carried out on Solartron Analytical 1400 (AMETEK) at a scan rate of 0.01 mV·s^{-1} between 3.0 V and 2.0 V. The self-discharge performance was evaluated by storing batteries for 0, 1, 2, and 3 mo before discharging, or for an intermittence of 7 d after partial discharging.

Preparation of 1,5-DNN Electrodes for XRD Test. For XRD tests, 1,5-DNN freestanding electrodes were prepared by mixing 1,5-DNN, graphene, and polytetrafluoroethylene (PTFE) emulsions (10%, wt%) in a weight ratio of 6:3:1, then isopropanol (*i*-PP) was added. After stirring about 30 min, the mixture was dried in an oven at 50 °C. Another small amount of *i*-PP was added and slowly stirred with a spoon until the mixture changed to a gel state. The obtained mixture was rolled into film, then dried in a vacuum at 50 °C for 8 h.

Preparation of Carbon Paper Electrodes for Batteries Operated in CO_2 Atmosphere. 1,5-DNN, graphene and poly(vinylidene fluoride) were mixed in a ratio of 8:1:1 (wt%), then a small amount of *N*-methylpyrrolidone was added. The mixture was ball milled at 300 rpm for an hour. Then the slurry was dropped onto carbon paper (HCP010N) and dried at 50 °C for 8 h.

Materials Characterization. FTIR spectra were collected by a Bruker Alpha P spectrometer with reflection ATR module in emission from 4,000 cm^{-1} to 400 cm^{-1}. XPS was performed on a Thermo Fisher ESCALAB-250Xi+. The XRD pattern was recorded using Rigaku Altima IV with Cu Kα radiation (λ = 1.5406 Å) operating at 40 kV and 40 mA. UV-visible spectroscopy measurements were conducted on a Shimadzu UV-3600+. SEM (S4800) was used to detect the morphology of electrodes.

GC-MS Characterization. Ten discharged electrodes were placed in a 2-mL centrifuge tube. Then, 1 mL of chloroform was added, and the tube was sonicated for 5 min. After that, the solution was filtered with a PTFE membrane (0.22 μm, Agela Technologies). An additional 1 mL of H_2O was added to filtrate, and the resulting solution was vortexed for 1 min. The organic layer was carefully collected and subjected to GC-MS analysis. GC-MS analysis was carried out using a Thermo Trace 1310 ISQ with an Agilent VF-624 column (30 m × 0.32 mm, 0.25 μm). The software used for controlling and data processing was Chromeleon 7. Compounds were identified by their retention times and confirmed with National Institute of Standards and Technology MS Search 2.3 database. Electron ionization mode was applied at 70 eV. Helium was used as the carrier gas with a column flow of 1 mL·min^{-1}. One microliter of solution was directly injected into the GC inlet (200 °C). The temperatures of transfer line and ion source were 250 °C and 280 °C, respectively. The following oven temperature was kept at 100 °C for 1 min, and the temperature was increased to 280 °C at a rate of 10 °C·min^{-1} and held for 5 min.

Data Availability. All study data are included in the article and/or *SI Appendix*.

ACKNOWLEDGMENTS. We acknowledge the support of the National Natural Science Foundation of China (Grants 22179092 and 52073211) and the National Key Research and Development Program of China (Grant 2019YFE0118800). We thank D. Y. Wang and Dr. Y. Z. Fu (College of Chemistry, Zhengzhou University) for their help with mass spectrum characterization, as well as for general discussion. Also, we thank L. L. Ma (School of Materials Science and Engineering, Tianjin University) for her help with XPS measurements.

1. Y. Qiao *et al.*, A high-energy-density and long-life initial-anode-free lithium battery enabled by a Li_2O sacrificial agent. *Nat. Energy* **6**, 653–662 (2021).
2. C. Niu *et al.*, Balancing interfacial reactions to achieve long cycle life in high-energy lithium metal batteries. *Nat. Energy* **6**, 723–732 (2021).
3. W. Xue *et al.*, Ultra-high-voltage Ni-rich layered cathodes in practical Li metal batteries enabled by a sulfonamide-based electrolyte. *Nat. Energy* **6**, 495–505 (2021).
4. Q. Ma *et al.*, Formulating the electrolyte towards high-energy and safe rechargeable lithium-metal batteries. *Angew. Chem. Int. Ed. Engl.* **60**, 16554–16560 (2021).
5. Y. S. Hong *et al.*, Hierarchal defect engineering for $LiCoO_2$ through low-solubility trace element doping. *Chem* **6**, 2759–2769 (2020).
6. Z. Zhu *et al.*, A surface Se-substituted $LiCo[O_{2-\delta}Se_\delta]$ cathode with ultrastable high-voltage cycling in pouch full-cells. *Adv. Mater.* **32**, e2005182 (2020).
7. X. Li *et al.*, Enabling stable high-voltage $LiCoO_2$ operation by using synergetic interfacial modification strategy. *Adv. Funct. Mater.* **20**, 2004664 (2020).
8. A. R. Armstrong, P. G. Bruce, Synthesis of layered $LiMnO_2$ as an electrode for rechargeable lithium batteries. *Nature* **381**, 499–500 (1996).
9. X. Zhu *et al.*, $LiMnO_2$ cathode stabilized by interfacial orbital ordering for sustainable lithium-ion batteries. *Nat. Sustain.* **4**, 392–401 (2021).
10. F. Lin *et al.*, Metal segregation in hierarchically structured cathode materials for high-energy lithium batteries. *Nat. Energy* **1**, 15004 (2016).
11. X. Xu *et al.*, Radially oriented single-crystal primary nanosheets enable ultrahigh rate and cycling properties of $LiNi_{0.8}Co_{0.1}Mn_{0.1}O_2$ cathode material for lithium-ion batteries. *Adv. Energy Mater.* **9**, 1803963 (2019).
12. P. Yan *et al.*, Tailoring grain boundary structures and chemistry of Ni-rich layered cathodes for enhanced cycle stability of lithium-ion batteries. *Nat. Energy* **3**, 600–605 (2018).
13. S. Tu *et al.*, A polysulfide-immobilizing polymer retards the shuttling of polysulfide intermediates in lithium-sulfur batteries. *Adv. Mater.* **30**, e1804581 (2018).
14. T. Zhou *et al.*, Twinborn TiO_2-TiN heterostructures enabling smooth trapping-diffusion-conversion of polysulfides towards ultralong life lithium-sulfur batteries. *Energy Environ. Sci.* **10**, 1694–1703 (2017).
15. X. Q. Zhang *et al.*, Electrolyte structure of lithium polysulfides with anti-reductive solvent shells for practical lithium-sulfur batteries. *Angew. Chem. Int. Ed. Engl.* **60**, 15503–15509 (2021).
16. D. Y. Wang, Y. Si, W. Guo, Y. Fu, Electrosynthesis of 1,4-bis(diphenylphosphanyl) tetrasulfide via sulfur radical addition as cathode material for rechargeable lithium battery. *Nat. Commun.* **12**, 3220 (2021).
17. Z. Zhu, X. Shi, G. Fan, F. Li, J. Chen, Photo-energy conversion and storage in an aprotic Li-O_2 battery. *Angew. Chem. Int. Ed. Engl.* **58**, 19021–19026 (2019).
18. X. Chi *et al.*, A highly stable and flexible zeolite electrolyte solid-state Li-air battery. *Nature* **592**, 551–557 (2021).
19. K. Chen, D. Y. Yang, G. Huang, X. B. Zhang, Lithium-air batteries: Air-electrochemistry and anode stabilization. *Acc. Chem. Res.* **54**, 632–641 (2021).
20. C. Peng *et al.*, Ultrahigh-energy-density fluorinated calcinated macadamia nut shell cathodes for lithium/fluorinated carbon batteries. *Carbon* **153**, 783–791 (2019).
21. Y. Li *et al.*, Fluorinated multi-walled carbon nanotubes as cathode materials of lithium and sodium primary batteries: Effect of graphitization of carbon nanotubes. *J. Mater. Chem. A* **7**, 7128–7137 (2019).
22. C. Jiang *et al.*, Electrolyte-assisted dissolution-recrystallization mechanism towards high energy density and power density CF cathodes in potassium cell. *Nano Energy* **70**, 104552 (2020).
23. Z. Ding *et al.*, Reaction mechanism and structural evolution of fluorographite cathodes in solid-state K/Na/Li batteries. *Adv. Mater.* **33**, e2006118 (2021).
24. T. Yang, Y. Jung, The dependence of the electrochemical performance of ambient Li-SO_2 primary cells on the electrolyte solvent. *Int. J. Electrochem. Sci.* **11**, 8169–8176 (2016).
25. J. H. Wei *et al.*, Acetylene black loaded on graphene as a cathode material for boosting the discharging performance of Li/$SOCl_2$ battery. *Int. J. Electrochem. Sci.* **12**, 898–905 (2017).
26. H. Gao, Y. Li, R. Guo, B. M. Gallant, Controlling fluoride-forming reactions for improved rate capability in lithium-perfluorinated gas conversion batteries. *Adv. Energy Mater.* **9**, 1900393 (2019).
27. H. He *et al.*, Highly-efficient conversion of SF_6 via an eight-electron transfer process in lithium batteries. *Nano Energy* **72**, 104679 (2020).
28. C. Zhao *et al.*, In situ electropolymerization enables ultrafast long cycle life and high-voltage organic cathodes for lithium batteries. *Angew. Chem. Int. Ed. Engl.* **59**, 11992–11998 (2020).
29. S. Bai *et al.*, Permselective metal-organic framework gel membrane enables long-life cycling of rechargeable organic batteries. *Nat. Nanotechnol.* **16**, 77–84 (2021).
30. Y. Lu, J. Chen, Prospects of organic electrode materials for practical lithium batteries. *Nat. Rev. Chem.* **4**, 127–142 (2020).
31. C. Peng *et al.*, Reversible multi-electron redox chemistry of π-conjugated N-containing heteroaromatic molecule-based organic cathodes. *Nat. Energy* **2**, 17074 (2017).
32. M. Tang *et al.*, Tailoring π-conjugated systems: From π-π stacking to high-rate-performance organic cathodes. *Chem* **4**, 2600–2614 (2018).
33. T. Sun, J. Xie, W. Guo, D. Li, Q. Zhang, Covalent-organic frameworks: Advanced organic electrode materials for rechargeable batteries. *Adv. Energy Mater.* **10**, 1904199 (2020).
34. C. J. Yao *et al.*, Two-dimensional (2D) covalent organic framework as efficient cathode for binder-free lithium-ion battery. *ChemSusChem* **13**, 2457–2463 (2020).
35. H. Wang *et al.*, Recent progress in carbonyl-based organic polymers as promising electrode materials for lithium ion batteries (LIBs). *J. Mater. Chem. A* **8**, 11906–11922 (2020).
36. J. Yang *et al.*, Rational molecular design of benzoquinone-derived cathode materials for high-performance lithium-ion batteries. *Adv. Funct. Mater.* **30**, 1909597 (2020).
37. Y. Liang *et al.*, Heavily n-dopable π-conjugated redox polymers with ultrafast energy storage capability. *J. Am. Chem. Soc.* **137**, 4956–4959 (2015).
38. G. Dai *et al.*, The design of quaternary nitrogen redox center for high-performance organic battery materials. *Matter* **1**, 945–958 (2019).
39. P. Acker, L. Rzesny, C. F. N. Marchiori, C. M. Araujo, B. Esser, π-conjugation enables ultra-high rate capabilities and cycling stabilities in phenothiazine copolymers as cathode-active battery materials. *Adv. Funct. Mater.* **29**, 1906436 (2019).
40. W. Guo, Y.-X. Yin, S. Xin, Y. G. Guo, L. J. Wan, Superior radical polymer cathode material with a two-electron process redox reaction promoted by graphene. *Energy Environ. Sci.* **5**, 5221–5225 (2012).
41. Y. Lu *et al.*, Cyclohexanehexone with ultrahigh capacity as cathode materials for lithium-ion batteries. *Angew. Chem. Int. Ed. Engl.* **58**, 7020–7024 (2019).
42. J. Wang *et al.*, Conjugated sulfonamides as a class of organic lithium-ion positive electrodes. *Nat. Mater.* **20**, 665–673 (2021).
43. X. Liu, Z. Ye, Nitroaromatics as high-energy organic cathode materials for rechargeable alkali-ion (Li^+, Na^+, and K^+) batteries. *Adv. Energy Mater.* **11**, 2003281 (2020).
44. P. Sun *et al.*, A lithium-organic primary battery. *Small* **16**, e1906462 (2020).
45. A. L. Michan *et al.*, Fluoroethylene carbonate and vinylene carbonate reduction: Understanding lithium-ion battery electrolyte additives and solid electrolyte interphase formation. *Chem. Mater.* **28**, 8149–8159 (2016).
46. Y. Lee *et al.*, Fluoroethylene carbonate-based electrolyte with 1 M sodium bis(fluorosulfonyl)imide enables high-performance sodium metal electrodes. *ACS Appl. Mater. Interfaces* **10**, 15270–15280 (2018).
47. R. Wang *et al.*, Safety-reinforced rechargeable Li-CO_2 battery based on a composite solid state electrolyte. *Nano Res.* **12**, 2543–2548 (2019).
48. Z. Zhang *et al.*, Exploiting synergistic effect by integrating ruthenium-copper nanoparticles highly co-dispersed on graphene as efficient air cathodes for Li-CO_2 batteries. *Adv. Energy Mater.* **9**, 1802805 (2019).
49. H. Chen *et al.*, From biomass to a renewable $Li_xC_6O_6$ organic electrode for sustainable Li-ion batteries. *ChemSusChem* **1**, 348–355 (2008).
50. Z. Song *et al.*, Polyanthraquinone as a reliable organic electrode for stable and fast lithium storage. *Angew. Chem. Int. Ed. Engl.* **54**, 13947–13951 (2015).
51. Y. Liang, P. Zhang, J. Chen, Function-oriented design of conjugated carbonyl compound electrodes for high energy lithium batteries. *Chem. Sci. (Camb.)* **4**, 1330–1337 (2013).
52. W. Huang *et al.*, Quasi-solid-state rechargeable lithium-ion batteries with a calix[4]-quinone cathode and gel polymer electrolyte. *Angew. Chem. Int. Ed. Engl.* **52**, 9162–9166 (2013).
53. Z. Zhang *et al.*, Enhancing the electrochemical performance of a high-voltage $LiCoO_2$ cathode with a bifunctional electrolyte additive. *ACS Appl. Energy Mater.* **4**, 12954–12964 (2021).
54. X. Huang, Y. Yao, F. Liang, Y. Dai, Concentration-controlled morphology of $LiFePO_4$ crystals with an exposed (100) facet and their enhanced performance for use in lithium-ion batteries. *J. Alloys Compd.* **743**, 763–772 (2018).
55. J. Duan *et al.*, Enhanced electrochemical performance and thermal stability of $LiNi_{0.80}Co_{0.15}Al_{0.05}O_2$ via nano-sized $LiMnPO_4$ coating. *Electrochim. Acta* **221**, 14–22 (2016).
56. S. Chen *et al.*, Ni-rich $LiNi_{0.8}Co_{0.1}Mn_{0.1}O_2$ oxide coated by dual-conductive layers as high performance cathode material for lithium-ion batteries. *ACS Appl. Mater. Interfaces* **9**, 29732–29743 (2017).
57. J. Zhang *et al.*, Tuning oxygen redox chemistry in Li-rich Mn-based layered oxide cathodes by modulating cation arrangement. *Adv. Mater.* **31**, e1901808 (2019).
58. Y. Manabe, R. Yazami, Accurate state of charge assessment of lithium-manganese dioxide primary batteries. *J. Power Sources* **359**, 422–426 (2017).
59. D. Wang *et al.*, The effects of pore size on electrical performance in lithium-thionyl chloride batteries. *Front. Mater.* **6**, 245 (2019).
60. X. Ji, K. T. Lee, L. F. Nazar, A highly ordered nanostructured carbon-sulphur cathode for lithium-sulphur batteries. *Nat. Mater.* **8**, 500–506 (2009).